



THE UNIVERSITY *of* EDINBURGH

Edinburgh Research Explorer

Improved interlayer performance of short carbon fiber reinforced composites with bio-inspired structured interfaces

Citation for published version:

Zhang, M, Zhang, J, Yang, D, Li, Y, Cui, X & Fu, K 2024, 'Improved interlayer performance of short carbon fiber reinforced composites with bio-inspired structured interfaces', *Additive Manufacturing*, vol. 79, 103936. <https://doi.org/10.1016/j.addma.2023.103936>

Digital Object Identifier (DOI):

[10.1016/j.addma.2023.103936](https://doi.org/10.1016/j.addma.2023.103936)

Link:

[Link to publication record in Edinburgh Research Explorer](#)

Document Version:

Peer reviewed version

Published In:

Additive Manufacturing

General rights

Copyright for the publications made accessible via the Edinburgh Research Explorer is retained by the author(s) and / or other copyright owners and it is a condition of accessing these publications that users recognise and abide by the legal requirements associated with these rights.

Take down policy

The University of Edinburgh has made every reasonable effort to ensure that Edinburgh Research Explorer content complies with UK legislation. If you believe that the public display of this file breaches copyright please contact openaccess@ed.ac.uk providing details, and we will remove access to the work immediately and investigate your claim.



Improved interlayer performance of short carbon fiber reinforced composites with bio-inspired structured interfaces

Minghui Zhang^a, Junming Zhang^a, Dongmin Yang^b, Yan Li^a, Xiaoyu Cui^{a,†}, Kunkun Fu^{a,*}

^a School of Aerospace Engineering and Applied Mechanics, Tongji University, Shanghai
200092, PR China

^b Institute for Materials and Processes, School of Engineering, University of Edinburgh,
Edinburgh, EH9 3FB, UK

Abstract: The weak layer interfaces of 3D-printed short carbon fiber (SCF) reinforced polymer composites have remained an issue due to planar layer printing by traditional 3D printers. Recently, multi-axis 3D printing technology which can realize non-planar layer printing has been developed. This study's aim was to evaluate and compare the bonding performance of non-planar interfaces produced by multi-axis 3D printing with that of planar interfaces. The tested non-planar interfaces were designed as bio-inspired structured interfaces (BISIs) based on microstructural interfacial elements in biological materials. The standard specimens with the 0°/90° and 0° infill line directions were printed by a robotic arm multi-axis 3D printer. Double cantilever beam (DCB) and end-notched flexure (ENF) tests were conducted to obtain Mode I and Mode II interlaminar toughness of SCF-reinforced composites. Test results showed that the critical energy release rates of the integrally formed BISI were significantly improved compared with the planar interface (PLAI) for both Mode I and Mode II delamination. In particular, the BISI with 0° infill line direction exhibited the greatest increase in critical energy release rate, and the damaged areas were spatially swept through the curved interfaces of the BISI with different infill line directions by scanning electron microscopy (SEM) and computed tomography (CT), which showed that the higher critical energy release rate was always accompanied with a larger damaged area. In addition, the tensile and flexural properties of 0°-infilled PLAI and BISI specimens were also measured. This

*Corresponding author: K. Fu. E-mail address: 1984fukunkun@tongji.edu.cn

†Corresponding author: X.Y. Cui. E-mail address: cuixiaoyu@tongji.edu.cn

1 work provides an in-depth investigation of the PLAI and BISI properties of SCF-
2 reinforced composites, demonstrating the potential benefits of integrally formed BISI
3 by multi-axis 3D printing and fostering new perspectives to enhance layer interfaces of
4 3D printed composites.

5

6 **Keywords:** Multi-axis 3D printing; Bio-inspired structured interface (BISI); Interfacial
7 toughness; Short carbon fiber (SCF) reinforced composite.

1. Introduction

3D printing is an emerging technology in various industries due to its advantages of high automation, rapid prototyping, and the flexible production of complex structures without assembly [1-5]. Fused filament fabrication (FFF) is regarded as the most popular and efficient 3D printing method, because of its scalability as well as the flexibility of both material and design [6-9]. The mechanical properties of FFF printed parts mainly depend on three factors, i.e., material type, structural parameters (e.g. infill density, raster angle, printing orientation and stacking sequence), and manufacturing process parameters (e.g. printing speed, extrusion temperature and rate, nozzle transverse speed, and bed temperature) [10, 11].

Correspondingly, extensive studies [12-14] have been conducted to tailor these parameters to improve the mechanical properties of printed parts. Although widespread printed structures often exhibit poor mechanical properties because of the thermoplastic polymers used as feedstock materials in FFF printing, thermoplastic materials reinforced by short carbon fibers (SCFs), aramid fibers, glass fibers (GF) and other reinforcing particulates show improvement in mechanical properties [15-19]. However, the insufficient diffusion and randomization of polymer molecular chains as well as voids across the interface result in weak interlayer bonding between layers, thereby affecting the interfacial properties of printed parts [20]. Therefore, enhancement of the interfacial performance between layers is critical to improving the mechanical properties of FFF printed parts [21, 22].

In most published studies, optimizing the manufacturing process parameters of planar printing has been a common method to enhance the interlayer bonding [23, 24]. Liu *et al.* [25] systematically examined the effects of printing pressure on the mechanical properties of sized CF-reinforced polyamide-6 (PA-6). They showed that the interfacial performance enhancement became more significant with a greater printing pressure by decreasing the printing height. Tian *et al.* [26] and Wang *et al.* [27] also found a decrease in the thickness of the printing layer could improve the

1 fiber/matrix interfacial properties because it promoted the impregnation of the molten
2 resin matrix into the reinforcing fibers by increasing the compaction effect of the
3 printing nozzle on the filaments. Further, the compaction effect also improved the
4 interfacial bonding between the adjacent printed filaments and layers [28]. In addition,
5 temperature parameter was investigated as an important factor on the printing quality
6 in extensive studies [27, 29-35]. Wang *et al.* [27] studied the mechanical properties of
7 CF and GF-reinforced polyether ether ketone composites with different temperature
8 parameters. They found that increasing the temperature to 440 °C could improve the
9 bonding strength of interlayer interfaces, therefore, improving the mechanical
10 properties of printed parts. In addition, Seppala *et al.* [29] discovered that temperature
11 was a critical parameter in determining the mobility of polymer molecular chains,
12 especially for glassy polymers. Increasing the nozzle temperature and reducing the
13 printing speed could prolong the time for the filament to remain above its glass
14 transition temperature, thereby improving interlayer bonding [30]. Yin *et al.* [31]
15 experimentally investigated the effects of build stage temperature on the interfacial
16 bonding strength of a thermoplastic polyurethane (TPU)/acrylonitrile-butadiene-
17 styrene bi-material structure. The results showed that increasing the build stage
18 temperature has a significant effect on the thermal history of deposited filaments and
19 enhances the interfacial bonding strength. Numerous studies have showed that higher
20 printing temperatures can improve the interfacial properties and reduce the porosity of
21 printed parts, leading to better mechanical properties [32, 33]. However, excessively
22 high printing temperatures can cause excessive flow or the thermal decomposition of
23 polymers, reducing the deposition accuracy and impairing the properties of the printed
24 parts [34, 35].

25 In addition to the optimization of process parameters of the planar printing, some
26 researchers have taken alternative approaches to enhance the interfacial properties
27 between layers, such as laser-assisted heating [22], radio frequency technique [36], and
28 plasma treatment [37]. To further improve the interlayer performance, the establishment

of non-planar interfaces is a novel technique. A bio-inspired structured interface (BISI) was assembled by adhesive joint forming a non-planar interface [38-40]. A sutural structure in biological materials is composed of rigid suture teeth and compliant interface layers. As a microstructural interface element, it is typically found in areas where control of the inherent strength and flexibility of material interfaces is required [41, 42]. Therefore, based on the biomimetic mechanism of this microstructure, some researchers considered the bonding between the matrix and the reinforcing phase as rigid suture teeth, and the interfacial bonding between layers as compliant interface layers. A microstructure that resists crack propagation and interfacial failure in biology has been applied to practical structures, thereby improving their fracture resistance [43-45].

Through experimental and theoretical investigations, Cordisco *et al.* [46] compared the fracture behaviors along sine-patterned interfaces and planar interfaces (PLAI) in AA7075-T6 DCB specimens with adhesive joints. The results revealed that crack initiation and propagation were delayed in the BISI DCB specimens compared to the PLAI DCB specimens, and the peak load increased with the amplitude-to-wavelength ratio (A/λ). They also found that the intermittent crack growth promoted the critical energy release rate of the BISI DCB specimen, resulting in a serrated load-displacement behavior. Similarly, García-Guzmán *et al.* [38] used a FFF printing technique to experimentally and theoretically analyze the fracture resistance of adhesive joints in trapezoidal-patterned DCB specimens which were produced from nylon-glass fiber reinforced composites. The test results showed that the load exhibited a saw-tooth jump response when the crack propagated along the inclined part of the trapezoidal pattern. It was considered that there might be a mixed-mode fracture condition (adhesive/cohesive failure) in this region. In addition, cohesive failure of the substrate was also observed in the tests.

Naat *et al.* [39] summarized that there were four main failure mechanisms for this type of adhesive-based BISI: cohesive failure mode in the bondline, adhesive failure

1 mode within the interface, cohesive failure of the substrate, and mixed failure mode. To
2 prevent the possibility of cohesive failure of the substrate, Aranda *et al.* [40] placed
3 fibers around the contour of trapezoidal interface profiles and examined the effect of
4 printing direction on the fracture toughness of composite specimens that incorporated
5 BISI into their geometric design. The experimental results indicated a significant
6 increase in fracture toughness of BISI profiles printed in the vertical direction compared
7 with those printed in the horizontal direction.

8 From the aforementioned studies, it is clear that BISI plays a crucial role in
9 controlling the tortuosity of crack paths and improving the fracture resistance of the
10 interlaminar interface. However, these aforementioned specimens with BISI were
11 assembled from 3D printed components by adhesive joints, rather than integrated
12 molding, because traditional 3D printing techniques can only build structures through
13 planar layers. Recently, a multi-axis 3D printing technology has been developed to fully
14 exhibit the technological advantages of 3D printing for integrated molding [47-50]. Due
15 to its multi-axis motion characteristics, it can achieve non-planar printing and more
16 complex printed objects with curved interlaminar feature, eliminating the limitation of
17 degree of freedom present in traditional desktop 3D printers [51]. Therefore, in the
18 current study, we aimed to use a multi-axis 3D printing system to fabricate SCF-
19 reinforced composites with PLAI and BISI and evaluate its effectiveness in improving
20 the interlayer performance.

21 In this work, a robotic arm 3D printer with multi-axis printing capability was
22 constructed to realize the integrated deposition of the BISI, and its printing path was
23 controlled by a G-code algorithm to obtain the BISIs with 0/90° and 0° infill line
24 directions. DCB specimens and end-notched flexure (ENF) specimens with interface
25 types of PLAI and BISI were printed respectively with these two infill directions, and
26 the Mode I and Mode II delamination behaviors of two different interface types were
27 compared. The critical energy release rates of Mode I and Mode II were calculated and
28 the damaged region were characterized by scanning electron microscopy (SEM) and X-

ray computed tomography (CT). The damage mechanisms of the SCF-reinforced composites with curved interfaces were analyzed. Finally, the effect of curved interfaces on the tensile and flexural properties of the specimens were discussed.

2. Materials and methods

2.1. Equipment and materials

In this paper, a robotic arm 3D printer was successfully developed based on robotic arm equipment (ABB, Swiss) combined with a control module, as shown in **Fig. 1(a)**. Most parts of the printer head of this equipment, i.e., the movement module, feeding module, heating bed, and printing materials, are the same components as those of a traditional desktop 3D printer. The heating module was specially designed with a long cylindrical structure to prevent mutual interference and collision between the nozzle and the printed part during the multi-axis movement, as shown in **Fig. 1(b)**.

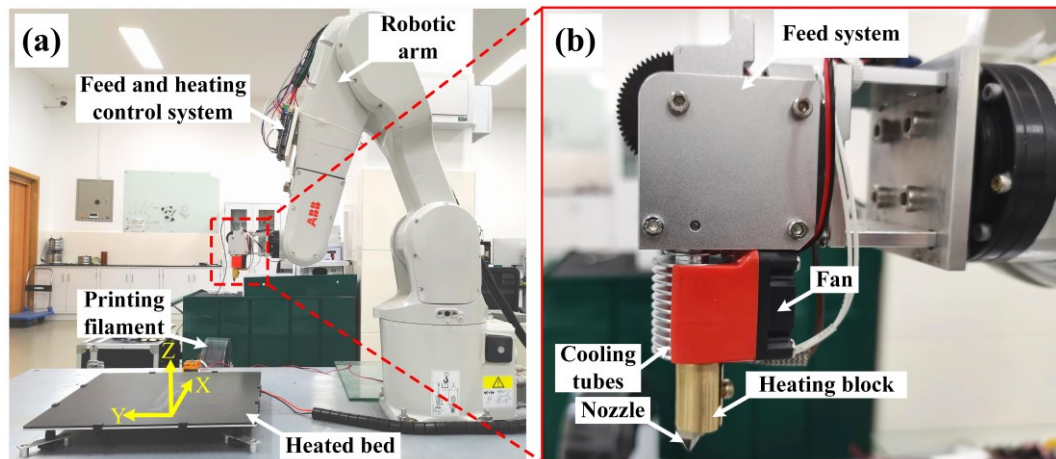


Fig. 1. Robot arm 3D printing equipment: (a) 3D printing equipment and printing module mounted on a robot arm, (b) printing nozzle and heating module.

In this study, an SCF-reinforced composite material (Onxy) supplied by Markforged (Massachusetts, USA) was used. Previous research demonstrated that Onyx was a mixture of chopped T300 CF and PA-6 plastic [52], and its filament diameter was 1.75 ± 0.05 mm [21]. Based on SEM measurements of the filament cross-sectional area after liquid nitrogen brittle fracture, as shown in **Fig. 2**, the chopped fiber diameter was approximately determined as 9 μ m, which was within the range of $(10 \pm 2$

1 μm) in the Markforged datasheet [53]. The SEM images indicated that the SCF
2 distribution in the matrix was relatively uniform, but there were still some tiny matrix
3 areas with insufficient SCF fillings, such as the yellow filled area in **Fig. 2**. In this study,
4 the filament was stored in a moisture-proof, sealed electronic desiccator (FCDE 1428B)
5 to prevent water uptake. In addition, to prevent any degradation of the filament that
6 could affect the mechanical properties of the materials, the filament was dried in an
7 eSUN filament storage box at 50 °C for one hour before printing. The printing
8 parameters of the Onyx materials using the aforementioned robotic arm 3D printer used
9 in this study are listed in **Table 1**.

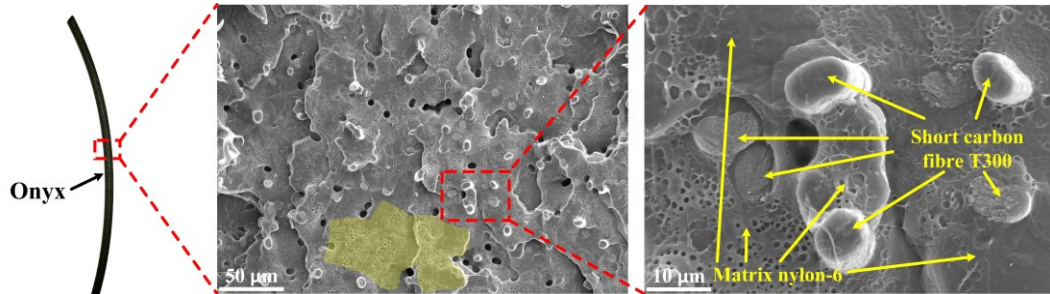


Fig. 2. Printing filament of Onyx and its SEM microscopic image.

Table 1

Robotic arm 3D printing parameters

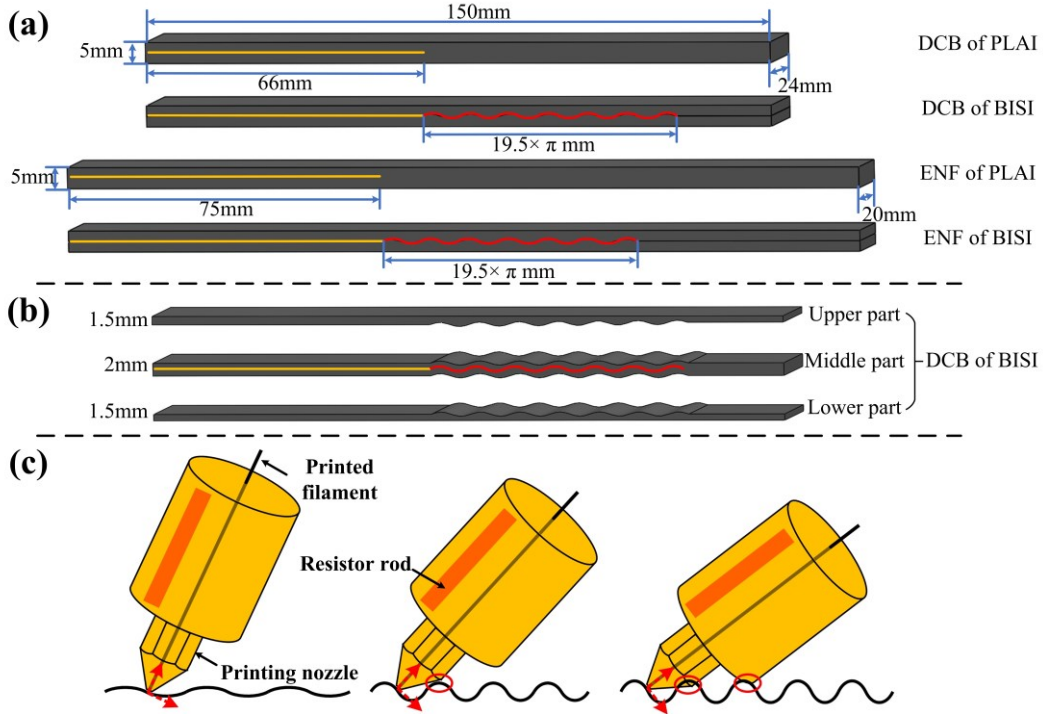
Parameters	Values	Units
Nozzle temperature	280	(°C)
Heating bed temperature	40	(°C)
Infill density	100	(%)
Infill line direction	[0/90], [0]	°
Line width	0.4	(mm)
Layer height	0.125	(mm)
Printing speed	30	(mm/s)
Wall layers	0.4	(mm)

2.2. Specimen preparation

2.2.1. Design of BISI specimen

To investigate the interlaminar toughness and interfacial failure characteristics of PLA and BISI between adjacent layers of Onyx, DCB specimens and ENF specimens

1 were printed using the multi-axis 3D printer according to ASTM D5528M-2021 [54]
 2 and ASTM D7905M-19 [55], respectively. The loading block used in this study is a
 3 piano hinge with a single edge length of 16mm. The geometries of the specimens are
 4 shown in **Fig. 3(a)**, where the pre-crack positions are indicated by the yellow line, and
 5 the shape and position of the BISIs are indicated by the red line. 0° and $0^\circ/90^\circ$ infilling
 6 patterns are two typical infilling patterns which has been widely used in 3D printing.
 7 These infilling patterns may result in either high longitudinal tensile properties or high
 8 interlaminar toughness. In this study, we aim to explore the mechanical performance of
 9 the specimens with and without curved interfaces. Hence, these two simple infilling
 10 patterns were selected to print the specimens for comparison.



11
 12 **Fig. 3.** Specimen size and motion interference diagram: (a) DCB and ENF specimens, (b) DCB
 13 specimen composition, (c) motion interference diagram.

14 The thickness of all four types of the specimens was set as 5 mm in **Fig. 3(a)**. To
 15 realize the 3D printing of the BISI layers with a sine function form, it was necessary to
 16 prepare a supportive base and perform top filling to create a standardized cuboid-shaped
 17 specimen. In this study, the standard specimen was partitioned into three parts: lower,
 18 middle, and upper, with careful consideration given to the distribution of thickness to

prevent the possibility of cohesive failure of the substrate. Taking the DCB specimens with BISI as an example, the thicknesses of the upper, middle, and lower parts were 1.5 mm, 2 mm, and 1.5 mm, respectively. The lower part acting as a base for the middle part was printed first using the traditional planar slicing method, then the middle part was multi-axis printed using a non-planar slicing method, and finally the upper part was sealed using the traditional planar slicing method, as shown in **Fig. 3(b)**. Different slicing methods were used to generate printing paths for the three parts of a specimen and the specimen was then printed together using the multi-axis 3D printer without pausing.

Multi-axis 3D printing requires the nozzle system to be perpendicular to the printing interface [56]. Therefore, when designing the multi-axis 3D printed BISI, it was necessary to consider whether the spatial movement of the nozzle system would clash with the previously deposited material of the printed part [57], as shown in **Fig. 3(c)**. To avoid interference and design a periodic BISI within a 5 mm thickness space, the trajectory of BISI was expressed by

$$Z = \sin(2/3 \times X) / 2 \quad (1)$$

where Z and X represented the point coordinates on the X -axis and Z -axis, respectively.

2.2.2. Multi-axis toolpath planning of BISI

Traditional FFF 3D printing toolpaths are composed of XYZ coordinates, nozzle speeds, and extrusion lengths. The FFF tool head is always limited to be perpendicular to the XY plane, although it allows the toolpaths to be controlled to reach any desired spatial coordinates. The printing path only needs the definition of the XY coordinates and the accumulation value of the Z-axis layer height. Hence, the printing interface generated by traditional 3D printing technology is a PLAI parallel to the XY plane. In contrast, the toolpath of multi-axis 3D printing can form any angle and direction with the XY plane, thus generating a non-PLAI [58].

In order to achieve this flexibility, the multi-axis toolpath planning must include the orientation information of nozzle (i.e. tool head) required for each coordinate. In

1 this field, most researchers use XYZ coordinates and quaternions to define the nozzle
 2 position and orientation, and use reverse kinematics solvers to calculate the joint angles
 3 and axis positions of the robotic arm [57].

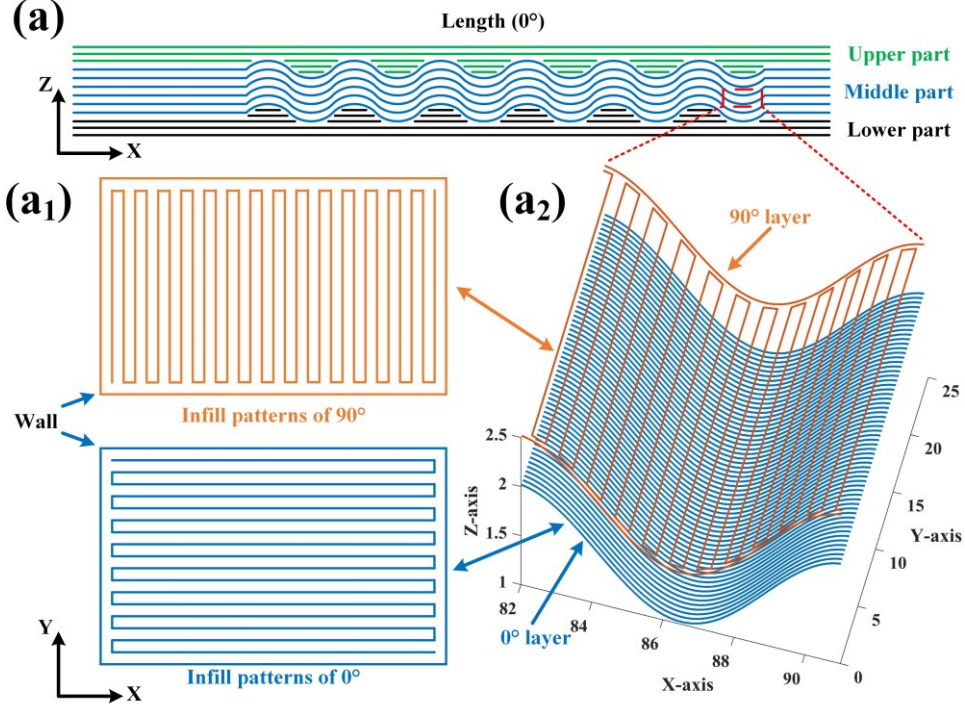


Fig. 4. Path planning for DCB of BISI: (a) schematic diagram of infill path, (a₁) 0°- and 90°-infill patterns by traditional slicing method, (a₂) 0/90°-infill path by non-planar slicing method.

To examine the effects of infill line direction and interface type on interlayer performance, a multi-axis toolpath planning algorithm is required to control the printing toolpath. Although various algorithms described in the existing literature can control the deposition direction of the tool, they are only applicable to surface geometries and are difficult to print standard interlayer fracture test specimens with a BISI [59-61]. In the algorithm adopted in this paper, the workpiece was first oriented to align its build direction with the global Z-axis, and then slicing was performed, similar to typical 3D printing deposition. The difference is that the Z-axis coordinates and directions were customized according to the trajectory required by the BISI, and then the XYZ coordinates and nozzle directions required for multi-axis 3D printing were generated. The required parameters of the manipulator were solved through quaternion and kinematics. Taking the DCB specimen with BISI with 0°/90° infill line directions

(represented as 0°/90°-infill BISI) as an example, the process is explained in detail as follows:

- a) For the lower part: First, the build direction was aligned in the global Z-axis. The part was sliced in the XY plane and stacked along the Z-axis, which was consistent with the traditional slicing method. However, the direction information of the nozzle needed to be additionally calculated. It should be noted that to ensure the surface quality and prevent thermal rebound of the specimen, the path generation included the brim of the first two layers.
- b) For the middle part: Based on the trajectory of the designed BISI, the relationship between the Z-axis coordinate and X was calculated using **Eq. (1)**. By taking the derivative of the function, the tangent angle and normal direction of the trajectory point were obtained, which represented the direction of the nozzle corresponding to the trajectory point of the BISI, expressed in **Eq. (2)**. Since the printed part had an infill line direction of 90°, the trajectory of **Eq. (1)** was divided into several arc lengths so that each arc length matched the line width, as shown in **Fig. 4(a) and Fig. 4(a2)**.

$$D_{head} = \arctan\left(-\frac{1}{\cos(X)/2}\right) \quad (2)$$

where D_{head} represents the direction of the nozzle.

- c) For the upper part: Because the Z-axis direction of this part had the characteristics of peaks and valleys, when printing this part, the valley should be filled until the height of the fillings was consistent with the height of the peak, so as to return to the XY plane interface form. Then, traditional slicing was performed on the part above the peak part. It should be noted that when filling the valley, the direction of the nozzle still needed to be considered since this was filling on the trajectory of the BISI.
- d) For the printing overall: Based on the XYZ coordinates and tool direction information obtained from the above algorithms, the XYZ coordinates and tool direction information required for the robotic arm 3D printer could be obtained by

quaternion and inverse motion solving algorithms, thereby achieving specimen printing. In addition, the infill pattern of the specimen is illustrated in **Fig. 4(a₁)**, and the X-axis, Y-axis, and Z-axis represent the length, width, and height directions of the specimen, respectively. The interior of each layer is infilled at a single angle. The 0°-infilled specimen is printed with an angle of 0°, and the 0°/90°-infilled specimen is printed alternately in 0° and 90°. Prior to the infilling of each layer, the printer prints along the outermost outline of that layer (called the wall) as shown in **Fig. 4(a₁)**. In addition, it is worth noting that when printing the upper part, a non-planar slicing method is required to generate the printing path of the wall.

2.2.3. Specimen printing

After obtaining the required data for the robotic arm 3D printer, the specimens with pre-crack were printed with the printing parameters listed in **Table 1**. The layer thickness of the specimens was set as 0.125 mm, with a total of 40 layers. To ensure that the pre-crack was located in the middle of the specimen, a thin film was placed on top of the 20th layer of the specimen. Since the pre-crack tip has a great influence on the test results [21], its thickness should be less than 0.013 mm according to the standard [54, 55]. In this study, a heat-resistant polyimide film with a thickness of 0.0125 mm was selected as the insert, as shown in **Fig. 5**. The flat film should be inserted at an accurate position and fixed to the edge of the specimen by solid adhesive to prevent the influence of thermal rebound of the deposited material on the print quality. The multi-axis 3D printing of the specimen with BISI was recorded in the video file in **Appendix**.

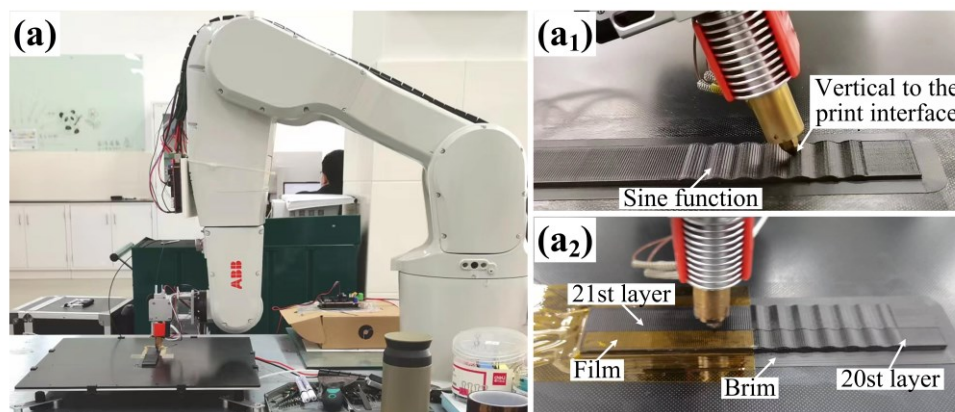


Fig. 5. The printing process for a specimen with a BISI.

2.3. Experimental tests

2.3.1. DCB and ENF tests

According to ASTM D5528M [54, 62], the DCB test was conducted at room temperature ($\sim 18^{\circ}\text{C}$) to obtain Mode I interlaminar toughness of specimens with PLAI and BISI. The test was performed using a Wance universal testing machine with a 5 kN load cell, and the crosshead speed was set as 2 mm/s. Because the low stiffness of the Onyx composite material may lead to a large displacement of the specimen during the crack growth process [35, 63-65], an aluminum plate with a thickness of 1.5 mm was used to reinforce the specimen, as shown in **Fig. 6(a)**. The surfaces of the aluminum plates and the specimens were polished to ensure bonding strength, and special precautions were taken during the reinforcement process to prevent any adhesive from entering the pre-crack and the sides of the specimen, which could potentially affect the test loading. Similar measures were taken to ensure the bonding strength between the loading block and the aluminum plate.

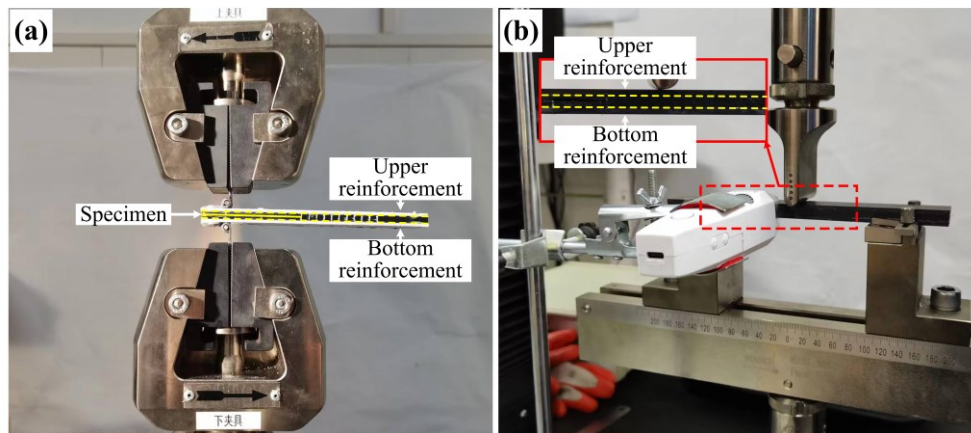


Fig. 6. DCB and ENF experimental setup: (a) DCB experimental setup, (b) ENF experimental setup.

According to ASTM D7905M [55, 66], the ENF test was performed using a three-point bending fixture on the same testing machine at room temperature, where the span L was 100 mm and the loading speed was 0.5 mm/s. Before the test, the tip of the pre-crack was marked on the specimen and three compliance calibration points (CC marks) were marked in the pre-crack area at 20 mm (right), 30 mm (middle), and 40 mm (left)

from the crack tip. First, during the test, the right and left CC marks were successively aligned with the centerline of the left support end in the three-point bending fixture, the loading indenter was loaded to a subcritical level, unloaded at a constant speed, and the load and displacement were recorded throughout the test, respectively. Then, the middle CC marker was aligned with the centerline of the left support end in the three-point bending fixture and again loaded for the test until cracks initiated. Due to the difficulty of observing crack initiation, in this experiment, a microscope was used to monitor and record the crack tip area in real time, as shown in **Fig. 6(b)**. To avoid local crushing or delamination under pressure of the contact area between the loading head and the specimen before crack initiation during the test, 2 mm thickness CF/PP fabric laminates were pasted on both sides of the specimen for reinforcement with the same bonding precautions as for the DCB specimen [21, 64, 67].

2.3.2. Tensile test and flexural test setup

To determine the tensile and flexural properties of the 0°-infilled PLA and 0°-infilled BISI specimens, the specimens were prepared using the multi-axis 3D printer by the same printing parameters and slicing methods as DCB and ENF specimens. The dimensions of the specimens were 120 mm×13.6 mm×5 mm and the length of the curved interfaces locating in the middle of the BISI specimens was approximately 108 mm. The tensile and flexural tests were performed using a Wance universal testing machine with a 5 kN load cell. The tensile tests were performed on the specimens with a crosshead speed of 2 mm/s at room temperature (~18°C) as shown in **Fig. 7.(a)**, and the displacement was monitored with an extensometer. The flexural tests were carried out at room temperature using a three-point bending apparatus with a span of 80 mm as shown in **Fig. 7.(b)**, and the crosshead speed was set as 2 mm/s.

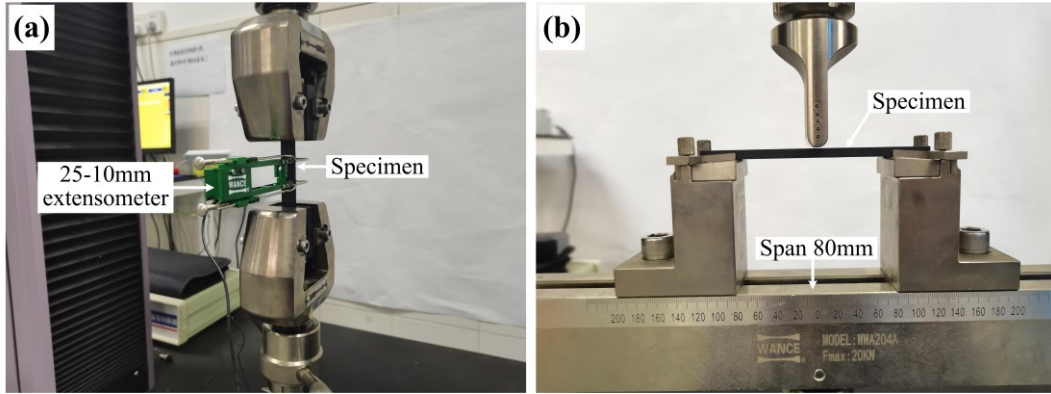


Fig. 7. Tensile and three-point bending experimental setup: (a) tensile experimental setup, (b) three-point bending experimental setup.

2.3.3. Microscopic characterization

The focus of this study was to investigate the interfacial behavior of $0^\circ/90^\circ$ -infill and 0° -infill BISIs, which was analyzed and characterized using SEM and CT scanning. First, small rectangular blocks were cut from printed specimens in different infill line directions. The cross-sections of blocks perpendicular to the longitudinal direction were obtained after brittle fracture in liquid nitrogen. This ensured that the cross-section remained clean and free of oil stains, and produced flat opposite surfaces. To improve its conductivity and scanning quality, each specimen was fixed on the specimen stage using conductive adhesive and subjected to sputtering gold plating treatment.

The microstructure and SCF distribution of the BISI were observed using an S-3400N scanning electron microscope, and the SCF direction trends were extracted by X-ray micro-CT (micro-CT, NanoVoxel 3000). The X-ray micro-CT scanning was performed with a resolution of 12 microns at a voltage of 10 kV and a current of 100 mA. The exposure time was 0.2 s. Then, the characteristics of the fractured interface were captured. The failure locations of the specimens with BISI were cut without altering the original failure morphology, and the microscopic fracture characteristics of the different infill line directions of the fracture specimens were observed and analyzed. Then, CT scans were performed and Avizo software was used to slice rectangular blocks of the same size (23 mm×8.5 mm) from the scan results, with the gold-plated area extracted by taking advantage of the different densities between Onyx and the sputtered

gold-plated materials, to observe the damaged areas.

3. Results and discussion

3.1. Microscale evaluation of specimens with BISI

Fig. 8(a) shows a schematic diagram of a suture structure in biomaterials, which is a symbolic structure with strong fracture resistance in the microscopic interface structure and is also the motivation of this paper [41, 43]. **Fig. 8(b)** shows the internal print quality of Onyx specimens with the $0^\circ/90^\circ$ -infill BISI, clearly demonstrating the sine function bond-lines of BISI and the arranged elliptical filaments. There are some gaps between the printed filaments with the 90° -infill layer. As shown in the image with a scale of $100\ \mu\text{m}$, the SCFs are exposed and pull-out occurs due to brittle fractures. The distribution of SCFs in the printed filament is relatively uniform, and a more obvious boundary line can be seen in the interface area between the upper and lower layers.

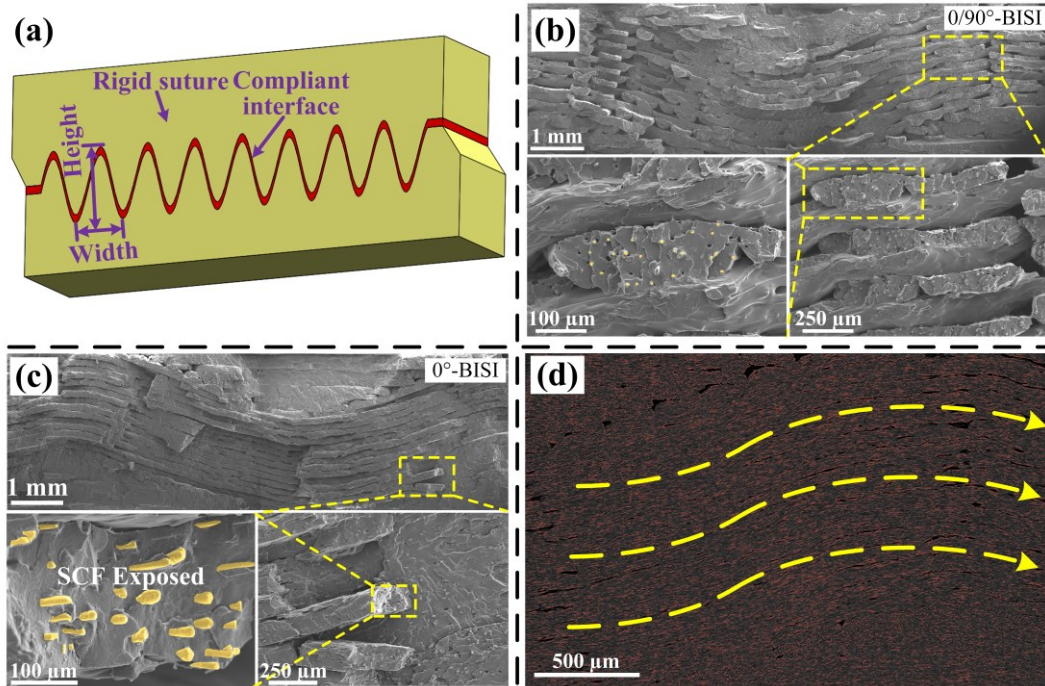


Fig. 8. Characterization of specimens with BISI: (a) diagram of sutured interfaces displaying the rigid sutures and a compliant interface, (b) SEM of $0^\circ/90^\circ$ -infill specimens, (c) SEM of 0° -infill specimens, (d) CT scanning of 0° -infill specimens.

Fig. 8(c) shows the internal printing quality of the 0° -infill BISI Onyx specimen,

clearly indicating the sine function trend of the BISI and a large number of exposed SCFs. The distribution uniformity of SCFs is poor compared with that of the raw material before printing (c.f. **Fig. 2**). However, the orientation of the SCFs is almost consistent with the infill line direction [68]. This is confirmed by the CT scan analysis and SCFs trend distribution, as shown in **Fig. 8.(d)**.

3.2. Results of fracture tests

3.2.1. Mode I fracture toughness

This section presents and compares the results of the DCB tests of PLA_I and BISI specimens with different infill line directions. To compare the force histories of different interface patterns, **Fig. 9(a)** and **Fig. 9(b)** display the force-displacement curves for the 0°/90°-infill and 0°-infill PLA_I and BISI specimens, respectively. It was found that the maximum forces of the 0°/90°-infill and 0°-infill BISI specimens are 35% and 85% higher than those of the PLA_I specimens, respectively. In addition, it is found that the delamination initiation of the BISI DCB specimens is delayed compared to the PLA_I specimens, which leads to high inter-laminar toughness. As the crack propagates along the curved interface highlighted in red as seen in the insert in **Fig. 9(b)**, the crack growth rate decreases and thus the released energy increases when the crack path approaching to the loading direction. In contrast, the crack growth rate is accelerated and thus the released energy decreases when the crack path (highlighted in black in the insert in **Fig. 9(b)**) deviates to the loading direction. Correspondingly, the crack jumping is seen in the BISI specimen. This phenomenon is also consistent with the observations as reported in the literature [40, 46]. Moreover, in **Fig. 9(a)** and **Fig. 9(b)**, it is worth noting that the integrally formed BISI specimens exhibit significant load fluctuation due to the unstable delamination propagation. Large force and energy are required for the delamination propagation compared to the PLA_I specimen. Therefore, it can be concluded that the BISI specimens demonstrate superior inter-laminar crack resistance.

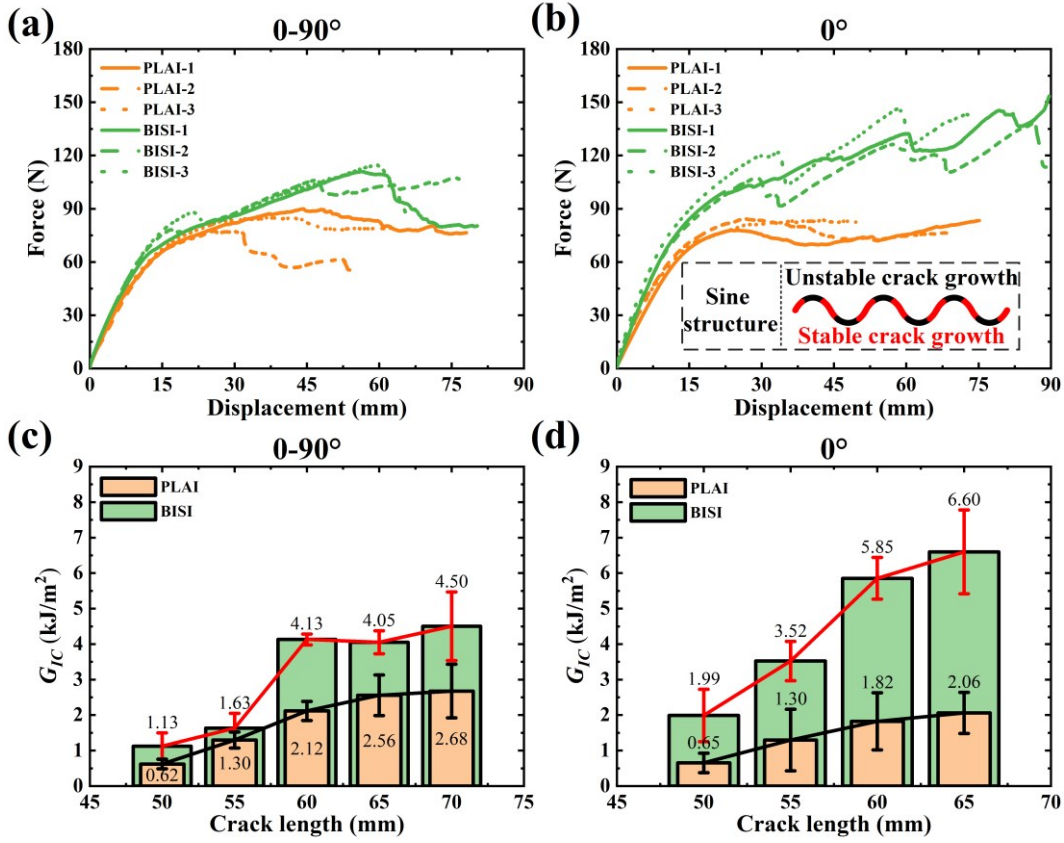


Fig. 9. DCB test results: (a) force-displacement curves of 0°/90°-infill PLA-I and BISI specimens, (b) force-displacement curves of 0°-infill PLA-I and BISI specimens, (c) R curves of 0°/90°-infill PLA-I and BISI specimens, (d) R curves of 0°-infill PLA-I and BISI specimens.

The critical energy release rate was calculated using the modified beam theory as:

$$G_{IC} = \frac{3P\delta}{2b(a + |\Delta|)} \frac{F}{N} \quad (3)$$

where P is the applied load. δ is the linear deflection. b is the width of the specimen. a is the delamination length. Δ is a crack length correction for crack tip rotation and deflection. F is the large displacement correction factor, and N is the large displacement and loading block correction factor. According to the ASTM D5528M [54], F and N are expressed as:

$$F = 1 - \frac{3}{10} \left(\frac{\delta}{a} \right)^2 - \frac{3}{2} \left(\frac{\delta t}{a^2} \right) \quad (4)$$

$$N = 1 - \left(\frac{L}{a} \right)^3 - \frac{9}{8} \left[\left(1 - \left(\frac{L}{a} \right)^2 \right) \right] \left(\frac{\delta t}{a^2} \right) - \frac{9}{35} \left(\frac{\delta}{a} \right)^2 \quad (5)$$

where t is the vertical distance from the center of the pin hole to the mid-plane of the

specimen arm, and L is the horizontal distance from the center of loading-block pin hole to the edge of the loading block. For piano hinge, $L=0$.

The G_{IC} of the $0^\circ/90^\circ$ -infill and 0° -infill PLA and BSI specimens are calculated and plotted in **Fig. 9(c)** and **Fig. 9(d)**. The results show that the fracture toughness of the specimens is improved by BSI compared with the traditional PLA. Specifically, the $G_{IC(0)}$ for delamination initiation of the $0^\circ/90^\circ$ -infill and 0° -infill BSI increased by 80.87% and 205.31%, respectively, with an averaged improvement of 65.66% and 204.52% in G_{IC} . These obtained data clearly demonstrate that BSI by multi-axis 3D printing can significantly improve the delamination resistance of specimens.

Previous studies claimed that although the adhesive-based BSI can improve the crack resistance of the specimens [38, 40, 46]. In **Fig. 9(a)** and **Fig. 9(b)**, it is worth noting that the integrally formed BSI specimens exhibit significant load fluctuation due to the unstable delamination propagation. Large force and energy are required for the delamination propagation compared to the PLA specimen. Therefore, it can be concluded that the BSI specimens demonstrate superior inter-laminar crack resistance.

3.2.2. Mode II fracture toughness

The results of the ENF test are depicted in **Fig. 10**. **Fig. 10(a)** and **Fig. 10(b)** illustrate the force-displacement curves for the $0^\circ/90^\circ$ -infill PLA and BSI specimens with $a = 30$ mm, respectively. The time for pre-crack propagation is marked by a five-pointed star, which is determined by carefully observing the test video recorded by the microscope.

The loading of the PLA specimens demonstrates almost linear growth until the initiation of pre-crack propagation, followed by a nonlinear force-displacement relationship, indicating steady crack growth. In contrast, the loading of the BSI specimens demonstrates primarily linear progression, even after the pre-crack propagation occurs.

The force-displacement curves for the 0° -infill PLA and BSI specimens are depicted in **Fig. 10(c)** and **Fig. 10(d)**, respectively. The trends observed in these curves

are generally consistent with those of the 0°/90°-infill specimens. The main difference is that only a short nonlinear stage appears in the pre-crack propagation of the 0°-infill PLAII specimens, followed by another linear increase in load. Furthermore, it is important to emphasize that the infill line direction has a significant impact on the fracture performance of the Mode II interface because the pre-crack propagation direction is perpendicular to the orientation of the SCFs in the 90° layers, and the debonding between adjacent printed 90° filaments is more likely to occur than the fracture of the 0° printed filament itself.

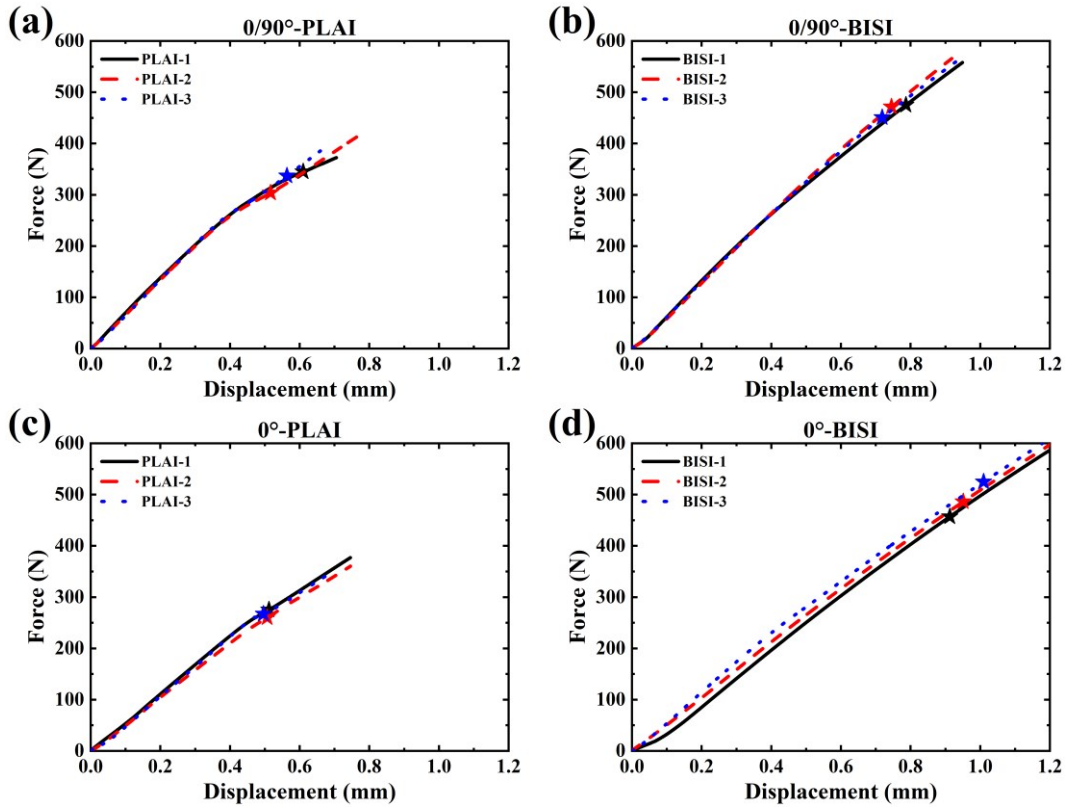


Fig. 10. ENF test results: (a) force-displacement curves for 0°/90°-infill PLAII specimens, (b) force-displacement curves for 0°/90°-infill BISI specimens, (c) force-displacement curves for 0°-infill PLAII specimens, (d) force-displacement curves for 0°-infill BISI specimens.

The Mode II interlaminar toughness (G_{IIC}) of composites can be calculated by

$$G_{IIC} = \frac{3mP_{\max}a_0}{2b} \quad (6)$$

where P_{\max} is the maximum load identified in the experiment. a_0 (i.e., 30 mm) is the crack length used in the test, and m is the compliance calibration coefficient, which is

determined by a linear least squares linear regression analysis on the compliance, C , versus crack length cubed (a^3) data

$$C = A + ma^3 \quad (7)$$

where the three compliances are those from the two compliance calibration tests (at $a = 20$ and 40 mm) and from the fracture test ($a_0 = 30$ mm).

Based on **Eq. (7)**, the slope m can be obtained by fitting the compliance obtained from the ENF test and the cube of the crack length. By combining the experimental data of the initial crack position and substituting it into **Eq. (6)**, the Mode II fracture toughness, G_{IIc} , is calculated. A comparison of G_{IIc} values between the $0^\circ/90^\circ$ -infill and 0° -infill PLA and BISI specimens is presented in **Fig. 11**. The results show that compared with the PLA specimens, the G_{IIc} values of the BISI specimens increased by 217% and 274%, respectively. It can be seen that BISI plays a crucial role in controlling the tortuosity of corresponding crack paths for fracture response.

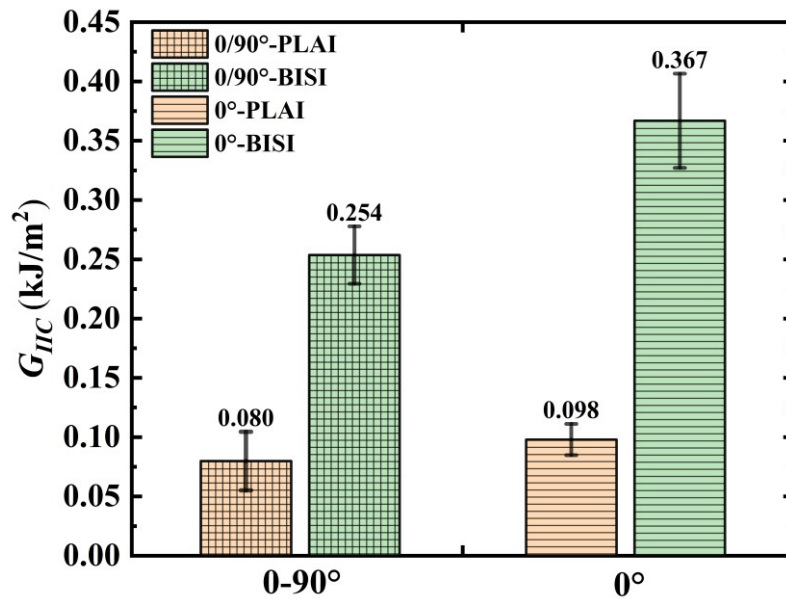


Fig. 11. Comparison of PLA and BISI specimens G_{IIc} with different infill line directions.

3.3. Fracture characterization and failure analysis

3.3.1. Failure analysis of DCB specimens

After the DCB test, microscopy scanning and analysis were performed on the failure surfaces of several test specimens. **Fig. 12** shows the macroscopic failure phenomena and SEM microscopic morphologies of PLA specimens with different

infill line directions. Specifically, **Fig. 12(a)** and **Fig. 12(b)** show two different interfacial crack growth phenomena of the $0^\circ/90^\circ$ -infill PLA specimens: interlaminar debonding and cross-layer debonding at the interface. Interlaminar debonding is a typical interfacial crack growth phenomenon (as shown by PLA-2 curve in **Fig. 9(a)**) [21]. From the SEM image of the damaged area (**Fig. 12(a₁)**), two clear traces of debonding of the 0° printed filament and the 90° layer (pick dash-dot line) can be seen. In the zoomed-in images (**Fig. 12(a₂)** and **Fig. 12(a₃)**), numerous exposed SCFs (yellow arrows) and SCF pull-out (blue arrows) can be observed. These observations indicate that interlaminar debonding is caused by the disruption of the matrix and the short fiber-matrix [62]. Because the peeling and shearing stress acts on each layer, when there are some printing defects on the interface or the local resin-rich region at the interface caused by the uneven distribution of SCFs, this can lead to the phenomenon of cross-layer debonding, which alters the crack propagation trajectory and improves the crack resistance performance of the specimen [21, 69]. In addition, **Fig. 12(b₂)** and **Fig. 12(b₃)** show that when the detached layer is fractured, this also involves the damage of the matrix and the fiber-matrix interface.

Fig. 12(c) shows the bridging phenomenon of printed filaments that occurs when the interface of the 0° -infill PLA specimens fails. This phenomenon involves the peeling of the matrix at the junction between the printed filaments, increasing the energy absorption during crack propagation. However, compared to the cross-layer debonding, bridging of the printed filament has less impact on delamination resistance (as indicated in **Fig. 9(c)** and **Fig. 9(d)**). Another important observation illustrated in **Fig. 12(c₁)**, **Fig. 12(c₂)**, and **Fig. 12(c₃)** is the presence of a significant number of SCFs distributed on the upper layer of the printed bridging filaments, while only a few instances of SCF pull-outs are visible on the lower layer. This can be explained by the fact that when the SCFs are densely distributed, the interlayer bonding strength is stronger. Consequently, when SCFs are distributed unevenly in the adjacent interlayers, the matrix and fiber-matrix interface are damaged at the interlaminar regions with

sparingly distributed SCFs, leading to differences in the degree of crack propagation between adjacent layers. Additionally, weak interface performance between 3D printed filaments results in the occurrence of filament bridging.

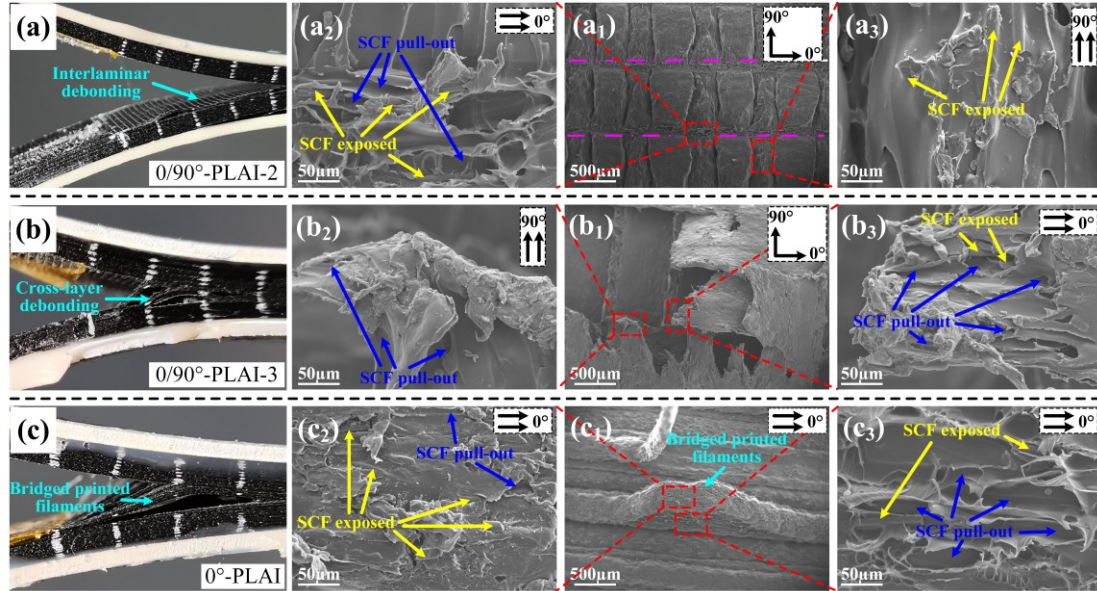
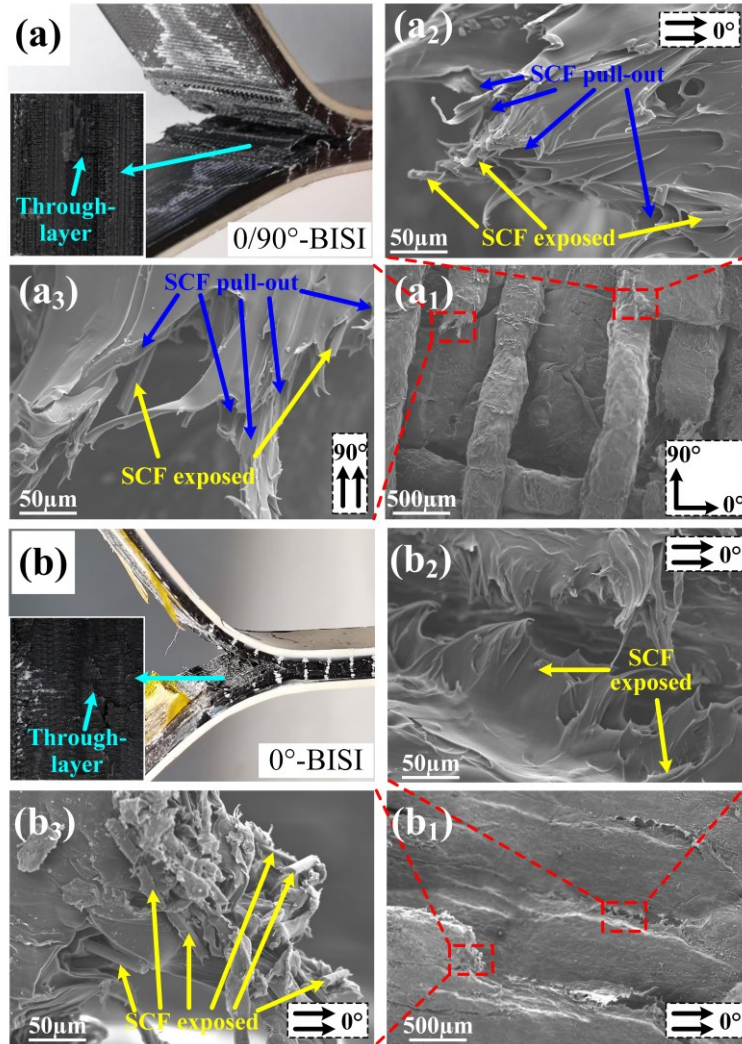


Fig. 12. Macroscopic failure modes and SEM image of different PLA-I specimens: (a) 0°/90°-infill PLA-I-2 specimen, (b) 0°/90°-infill PLA-I-3 specimen, (c) 0°-infill PLA-I specimen.

Fig. 13 shows the macroscopic fracture surfaces and microscopic morphologies of the 0°/90°-infill and 0°-infill BISI specimens after tests. It can be observed that since the printing interfaces adopt a spatially structured design, the crack propagation path in the specimen with BISIs roughly follows the trend of the set sine function and different levels of through-layer damage occur. The occurrence of through-layer damage releases a large amount of energies during the tests, which can be reflected from the corresponding force-displacement curves. For instance, the first peak force of the 0°/90°-infill BISI specimens was significantly lower than that of the 0°-infill BISI specimens due to the occurrence of severe through-layer damage as seen on the initial fractured surface of the 0°/90°-infill BISI specimen (**Fig. 9(a)** and **Fig. 9(b)**). Then, more severe through-layer damages hinder the crack propagation in the interfaces of the 0°/90°-infill BISI specimen compared with the 0°-infill BISI specimen. Correspondingly, high-value fluctuated forces are seen on the 0°/90°-infill BISI specimen compared to those of the 0°-infill BISI specimen (**Fig. 9(a)** and **Fig. 9(b)**).

1 **Fig. 13.(a₁)** and **Fig. 13.(b₁)** show the SEM microscopic morphologies of the interface
2 debonding failure of the 0°/90°-infill and 0°-infill BISI specimens, respectively. It can
3 be observed from **Fig. 13.(a₁)** that the interface debonding failure of the 0°/90°-infill
4 BISI specimens is accompanied by the destruction of the 0°-infill and 90°-infill printed
5 filaments. This destruction causes the crack path to move toward the pre-crack direction,
6 resulting in obvious through-layer damage.



7 **Fig. 13.** Macroscopic failure modes and SEM image of different BISI specimens: (a) 0°/90°-infill
8 BISI specimens, (b) 0°-infill BISI specimens.

10 Observed under SEM (**Fig. 13(a₂)** and **Fig. 13(a₃)**), the matrix damage of the 90°-
11 infill layers is more significant. The crack propagation direction is perpendicular to the
12 printed filament and thus the longitudinal direction of SCFs in the 90°-infill layers [4].
13 Therefore, the SCFs in the layers provide little reinforcement against longitudinal crack

propagation. **Fig. 13(b₂)** and **Fig. 13(b₃)** show the interfacial debonding in the 0°-infill BISI specimens, accompanied by the occurrence of through-layer damages. Most through-layer damages are caused by the short fiber/matrix debonding failure within the printed filament, accompanied by a small amount of inter-printed filament matrix failure. The debonding failure of short fiber/matrix is caused by the following factors. Firstly, the imperfect extrusion of the printer leads to uneven thickness of the printed filament, thereby forming irregular gaps around the printed filaments (**Fig. 8(b)** and **Fig. 8(d)**). Furthermore, as depicted in **Fig. 2**, **Fig. 8(d)**, and **Fig. 12(c)**, the distribution of short fibers in both raw filament and printed filament exhibits a certain degree of non-uniformity, resulting in differences of local interfacial performance between adjacent layers. Therefore, crack may propagate through the gaps to the layers with weaker interface properties. When cracks propagate between adjacent layers, the shear stress may cause debonding failure of the short fibers/matrix within the printing filaments. There is a correlation between interface performance and SCFs orientation and distribution.

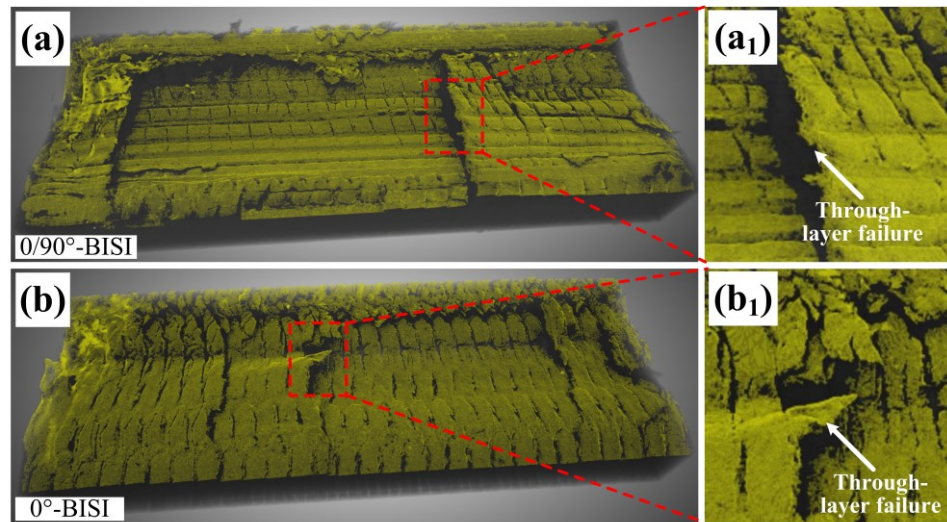


Fig. 14. Extraction of swept area of the interlayer crack.

Based on the analysis of the testing data and fracture morphology, the integrally formed BISI can significantly improve delamination resistance by controlling the direction and paths of delamination propagation [46, 69]. For Mode I fracture toughness, when the crack deviates from the pre-crack direction, the crack propagation slows down,

1 and the critical energy release rate increases significantly, which is consistent with the
2 results of the adhesive-based BISI. When the crack propagates along the pre-crack
3 direction, the increase in the G_{IC} is relatively smaller, but compared to adhesive-based
4 BISI, the amplitude of force attenuation is significantly reduced. Furthermore, during
5 delamination propagation, although both interfaces exhibit through-layer failure, the
6 through-layer damage level is smaller in the integrally formed BISI [38, 40].

7 Moreover, it should be emphasized that although the crack paths of the $0^\circ/90^\circ$ -
8 infill and 0° -infill BISI specimens are almost the same, there are significant differences
9 in the G_{IC} . In addition to the influence of the infill line direction, the variation of G_{IC} is
10 also caused by the difference of the degrees of the through-layer. In other words,
11 different levels of the through-layers damage lead to different failure damage areas
12 swept through the crack path, as shown in **Fig. 14**.

13 After processing with Avizo software, the surface area of the sprayed material was
14 extracted, and the areas swept through the cracks in the $0^\circ/90^\circ$ -infill and 0° -infill BISI
15 specimens were measured as 340 mm^2 and 424 mm^2 , respectively. It was observed that
16 the crack in the $0^\circ/90^\circ$ -infill specimen has a larger degree of through-layers compared
17 to the 0° -infill specimen, resulting in a smaller area swept through the crack path
18 compared to the theoretical area swept through the sine function. This difference in the
19 crack path area leads to a disparity in the G_{IC} .

20 3.3.2. Failure analysis of ENF specimens

21 **Fig. 15** displays the SEM images of the ENF specimens with $0^\circ/90^\circ$ -infill and 0° -
22 infill BISI. It is seen that, due to the presence of the BISI, the crack propagation
23 direction deviates from the pre-crack direction at a certain angle, while the crack path
24 still follows the designed sine function trajectory. In **Fig. 15(a)**, traces of matrix damage
25 (green arrow) can be observed in the $0^\circ/90^\circ$ -infill BISI specimen, while **Fig. 15(b)**
26 shows an occurrence of printed filament bridging similar to the DCB test when the 0° -
27 infill BISI specimen experiences shear forces, which also impedes crack propagation.
28 **Fig. 15(c)** illustrates the SEM images of fracture surfaces in the $0^\circ/90^\circ$ -infill and 0° -

infill PLA and BISI specimens. The yellow dashed lines with arrows indicate the direction of the matrix shearing, with the matrix being elongated along the direction of the arrow. It is evident that no traces of exposed SCFs or SCF pull-outs are observed in any of the four types of specimens, indicating weak shear resistance at the interface [21]. However, the BISI specimens exhibit a more damaged matrix on the fracture surface compared to the PLA specimens, suggesting a significant correlation between matrix damage and interfacial performance during Mode II fracture.

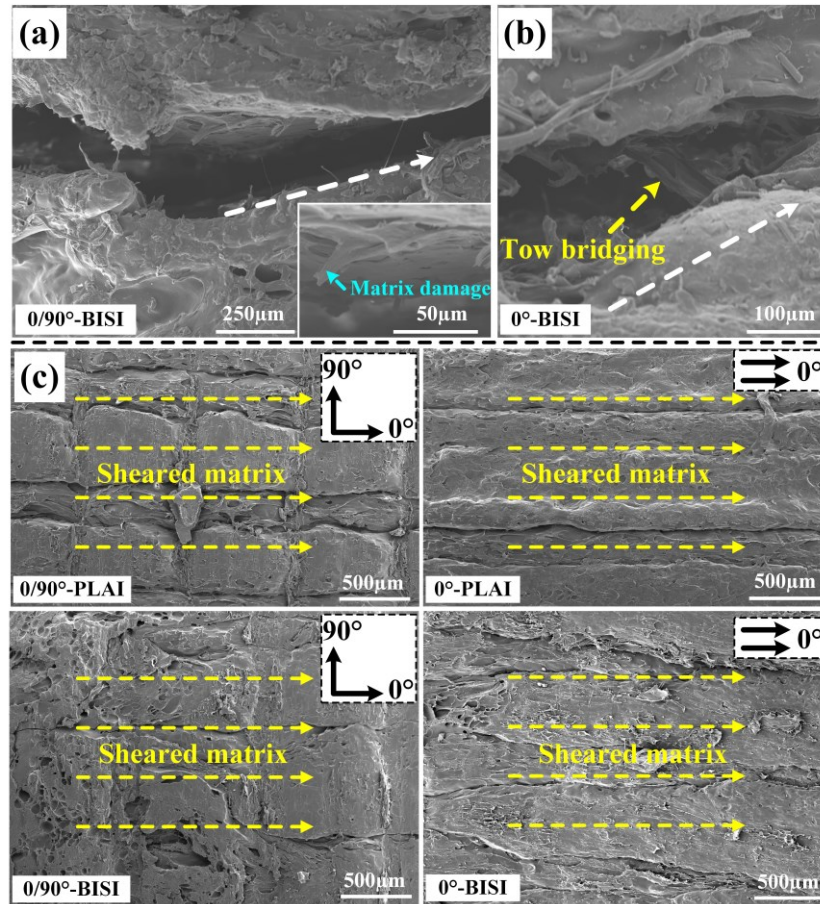


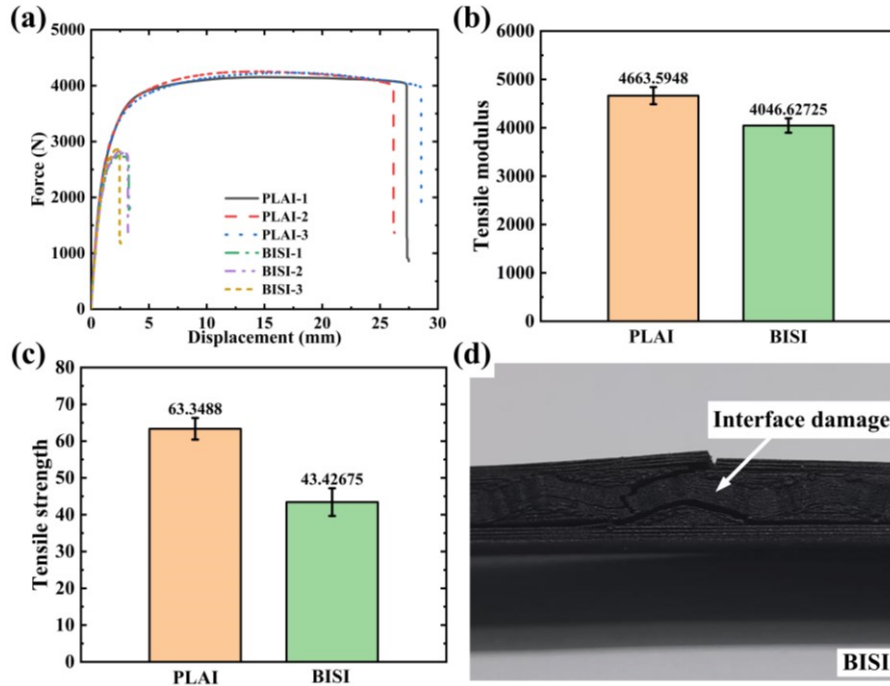
Fig. 15. SEM images of the fractured ENF specimens.

3.4. Tensile and flexural results

3.4.1. Tensile properties

Fig. 16(a) displays the tensile force-displacement curves of the 0°-infilled PLA and BISI specimens. It is found that the maximum force and the elongation at break of the 0°-infilled BISI tensile specimens are significantly lower than those of the 0°-infilled PLA specimens. Correspondingly, Fig. 16.(b) and Fig. 16.(c) show that the

1 0°-infilled BISI tensile specimens had an averaged 13.23% decrease in tensile modulus
 2 and an averaged 31.44% decrease in tensile strength compared to the 0°-infilled PLA
 3 specimens. In terms of 3D-printed SCF reinforced composites, more than 95% of fiber
 4 orientations is consistent with the printing path as reported in the literature [68].
 5 Therefore, aligned SCFs have a high reinforcing effect on the 0°-infilled PLA
 6 specimens. In contrast, the orientations of the SCFs in the 0°-infilled BISI specimens
 7 are not always consistent with the longitudinal direction due to the curved interfaces,
 8 resulting in the reduction in the tensile strength and modulus as seen in **Fig. 16(d)**. In
 9 other words, the curved interfaces of the specimens sacrificed the longitudinal tensile
 10 properties of the composites.



11
 12 **Fig. 16.** Tensile properties and fracture morphology of tensile specimens: (a) tensile force-
 13 displacement curves of 0°-infill PLA and BISI specimens, (b) tensile modulus of 0°-infilled PLA
 14 and BISI specimens, (c) tensile strength of 0°-infilled PLA and BISI specimens, (d) fracture
 15 morphology of 0°-infilled BISI specimen after test.

16 3.4.2. Flexural properties

17 **Fig. 17(a)** displays the force-displacement curves of the 0°-infill PLA and BISI
 18 specimens. The results indicate that the maximum forces of the 0°-PLA specimens are
 19 comparable to those of the 0°-BISI specimens. Correspondingly, the 0°-infilled BISI

flexural specimens had an averaged 2.33% decrease in flexural modulus and an averaged 4.01% decrease in flexural strength compared to the 0°-infill PLA-I specimens as shown in Fig. 17(b). The testing results show that the curved interfaces have little effect on the flexural properties of the composites.

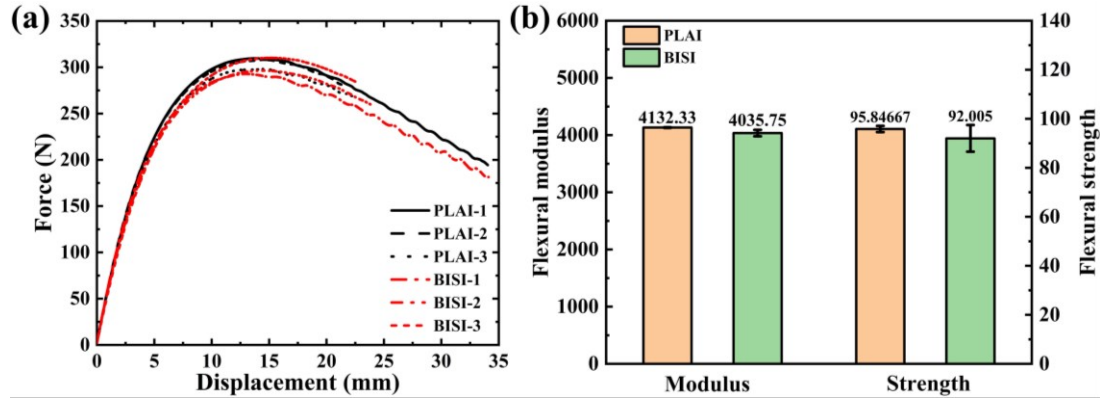


Fig. 17. Three-point bending test results: (a) force-displacement curves of 0°-infill PLA-I and BISI specimens, (b) flexural modulus and strength of the specimens.

4. Conclusions

In this study, the interlayer structure of the 3D printed SCF composites was designed with inspiration from bionics, and a multi-axis 3D printing algorithm was developed to realize the BISI specimen preparation. Mode I and Mode II fracture toughness tests were performed on the 0°/90°-infill and 0°-infill PLA-I and BISI specimens, and the microscopic morphology and damage area of the specimens after the test were characterized by SEM and CT scanning. By investigating the effects of infill line directions and the interfacial types on the interface properties of PLA-I and BISI printed specimens, the following conclusions were drawn:

- 1) Cross-layer debonding and printed filament bridging are observed when the PLA-I specimens failed after DCB tests. These phenomena are closely related to the distribution of SCFs and can effectively resist further crack propagation. Therefore, the Mode I interfacial failure is significantly related to the SCFs' direction.
- 2) When the integrally formed BISI specimens are observed after DCB tests, the crack path is consistent with the designed sine function trajectory. This demonstrates that

by controlling the tortuosity of the BISI, it is possible to provide a preferred path for the crack propagation and thus enhance the delamination resistance.

3) The failure process of the BISI specimens is accompanied by through-layer failure.

This phenomenon causes the crack to deviate from the pre-designed sine function track and slows down the tortuosity of the crack path, which is not conducive to the improvement of the fracture resistance of the structured interface.

4) The Mode II fracture toughness between two adjacent layers, as obtained by the ENF test, is relatively low, indicating poor shear resistance between the Onyx layers. However, the BISI can achieve a two-fold improvement in Mode II fracture toughness by optimizing the crack propagation path.

5) Tensile and flexural tests indicated that the curved interface sacrificed the longitudinal tensile properties of the composites but had little effect on the flexural performance.

Data availability

The authors do not have permission to share data.

Declaration of competing interest

The authors declare that they have no known competing financial interests or personal relationships that could have appeared to influence the work reported in this paper.

Acknowledgments

The authors at Tongji University would like to acknowledge the financial support from the National Key Research and Development Plan, P.R. China (grant number: 2022YFB4602000).

References

- [1] A. Entezari, N.-C. Liu, Z. Zhang, J. Fang, C. Wu, B. Wan, M. Swain, Q. Li, Nondeterministic multiobjective optimization of 3D printed ceramic tissue scaffolds, *J. Mech. Behav. Biomed. Mater.* 138 (2023) 105580. <https://doi.org/10.1016/j.jmbbm.2022.105580>.
- [2] S. Liu, Y. Li, N. Li, A novel free-hanging 3D printing method for continuous carbon fiber reinforced thermoplastic lattice truss core structures, *Mater. Des.* 137 (2018) 235-244. <https://doi.org/10.1016/j.matdes.2017.10.007>.
- [3] S. Bhandari, R.A. Lopez-Anido, D.J. Gardner, Enhancing the interlayer tensile strength of 3D printed short carbon fiber reinforced PETG and PLA composites via annealing, *Addit. Manuf.* 30 (2019) 100922. <https://doi.org/10.1016/j.addma.2019.100922>.
- [4] H. Zhang, S. Wang, K. Zhang, J. Wu, A. Li, J. Liu, D. Yang, 3D printing of continuous carbon fibre reinforced polymer composites with optimised structural topology and fibre orientation, *Compos. Struct.* 313 (2023) 116914. <https://doi.org/10.1016/j.compstruct.2023.116914>.
- [5] Z. Chen, Y. Li, S. Zhang, P. Wei, X. Dang, X. Jiang, B. Lu, Hierarchical architecture and mechanical behavior of K418 Ni-based superalloys manufactured by laser powder bed fusion, *Mat. Sci. Eng. A* 851 (2022) 143630. <https://doi.org/10.1016/j.msea.2022.143630>.
- [6] V. Shanmugam, D.J.J. Rajendran, K. Babu, S. Rajendran, A. Veerasimman, U. Marimuthu, S. Singh, O. Das, R.E. Neisiany, M.S. Hedenqvist, F. Berto, S. Ramakrishna, The mechanical testing and performance analysis of polymer-fibre composites prepared through the additive manufacturing, *Polym. Test.* 93 (2021) 106925. <https://doi.org/10.1016/j.polymertesting.2020.106925>.
- [7] H. Liu, K. Fu, H. Zhu, B. Yang, The acoustic property and impact behaviour of 3D printed structures filled with shear thickening fluids, *Smart Mater. Struct.* 31(1) (2022) 015026. <https://doi.org/10.1088/1361-665X/ac3b20>.

- [8] X. Tian, A. Todoroki, T. Liu, L. Wu, Z. Hou, M. Ueda, Y. Hirano, R. Matsuzaki, K. Mizukami, K. Iizuka, A.V. Malakhov, A.N. Polilov, D. Li, B. Lu, 3D printing of continuous fiber reinforced polymer composites: development, application, and prospective, *Chin. J. Mech. Eng.: Addit. Manuf. Front.* 1(1) (2022) 100016. <https://doi.org/10.1016/j.cjmeam.2022.100016>.
- [9] H.L. Ren, X.D. Yang, Z.H. Wang, X.G. Xu, R. Wang, Q. Ge, Y. Xiong, Smart structures with embedded flexible sensors fabricated by fused deposition modeling-based multimaterial 3D printing, *Int. J. Smart Nano Mater.* 13(3) (2022) 447-464. <https://doi.org/10.1080/19475411.2022.2095454>.
- [10] A. Cano-Vicent, M.M. Tambuwala, S.S. Hassan, D. Barh, A.A.A. Aljabali, M. Birkett, A. Arjunan, Á. Serrano-Aroca, Fused deposition modelling: Current status, methodology, applications and future prospects, *Addit. Manuf.* 47 (2021) 102362. <https://doi.org/10.1016/j.addma.2021.102378>.
- [11] Z. Zhang, Y. Long, Z. Yang, K. Fu, Y. Li, An investigation into printing pressure of 3D printed continuous carbon fiber reinforced composites, *Compos, Part A Appl. Sci.* 162 (2022) 107162. <https://doi.org/10.1016/j.compositesa.2022.107162>.
- [12] M. Samykano, S.K. Selvamani, K. Kadirgama, W.K. Ngui, G. Kanagaraj, K. Sudhakar, Mechanical property of FDM printed ABS: influence of printing parameters, *Int. J. Adv. Manuf. Tech.* 102(9) (2019) 2779-2796. <https://doi.org/10.1007/s00170-019-03313-0>.
- [13] I. Sedighi, M.R. Ayatollahi, B. Bahrami, M.A. Pérez-Martínez, A.A. Garcia-Granada, Mechanical behavior of an additively manufactured poly-carbonate specimen: tensile, flexural and mode I fracture properties, *Rapid Prototyping J.* 26(2) (2020) 267-277. <https://doi.org/10.1108/RPJ-03-2019-0055>.
- [14] R.R. Fernandes, A.Y. Tamijani, M. Al-Haik, Mechanical characterization of additively manufactured fiber-reinforced composites, *Aerosp. Sci. Technol.* 113 (2021) 106653. <https://doi.org/10.1016/j.ast.2021.106653>.
- [15] R.T.L. Ferreira, I.C. Amatte, T.A. Dutra, D. Bürger, Experimental characterization

1 and micrography of 3D printed PLA and PLA reinforced with short carbon fibers,
2 Compos, Part B: Eng. 124(1) (2017) 88-100.
3 <https://doi.org/10.1016/j.compositesb.2017.05.013>.

4 [16] M.A. Caminero, J.M. Chacón, I. García-Moreno, J.M. Reverte, Interlaminar
5 bonding performance of 3D printed continuous fibre reinforced thermoplastic
6 composites using fused deposition modelling, Polym. Test. 68 (2018) 415-423.
7 <https://doi.org/10.1016/j.polymertesting.2018.04.038>.

8 [17] W. Zhong, F. Li, Z. Zhang, L. Song, Z. Li, Short fiber reinforced composites for
9 fused deposition modeling, Mat. Sci. Eng. A 301(2) (2001) 125-130.
10 [https://doi.org/10.1016/S0921-5093\(00\)01810-4](https://doi.org/10.1016/S0921-5093(00)01810-4).

11 [18] T. Yu, Z. Zhang, S. Song, Y. Bai, D. Wu, Tensile and flexural behaviors of
12 additively manufactured continuous carbon fiber-reinforced polymer composites,
13 Compos. Struct. 225 (2019) 111147.
14 <https://doi.org/10.1016/j.compstruct.2019.111147>.

15 [19] Z. Yang, K. Fu, Z. Zhang, J. Zhang, Y. Li, Topology optimization of 3D-printed
16 continuous fiber-reinforced composites considering manufacturability, Compos.
17 Sci. Technol. 230 (2022) 109727.
18 <https://doi.org/10.1016/j.compscitech.2022.109727>.

19 [20] M.M. Garmabi, P. Shahi, J. Tjong, M. Sain, 3D printing of polyphenylene sulfide
20 for functional lightweight automotive component manufacturing through enhancing
21 interlayer bonding, Addit. Manuf. 56 (2022) 102780.
22 <https://doi.org/10.1016/j.addma.2022.102780>.

23 [21] X. Kong, J. Luo, Q. Luo, Q. Li, G. Sun, Experimental study on interface failure
24 behavior of 3D printed continuous fiber reinforced composites, Addit. Manuf. 59
25 (2022) 103077. <https://doi.org/10.1016/j.addma.2022.103077>.

26 [22] J. Zhang, W. Yang, Y. Li, Process-dependent Multiscale Modeling for 3D Printing
27 of Continuous Fiber-reinforced Composites, Addit. Manuf. (2023) 103680.
28 <https://doi.org/10.1016/j.addma.2023.103680>.

- 1 [23] J.M. Chacón, M.A. Caminero, P.J. Núñez, E. García-Plaza, I. García-Moreno, J.M.
2 Reverte, Additive manufacturing of continuous fibre reinforced thermoplastic
3 composites using fused deposition modelling: Effect of process parameters on
4 mechanical properties, *Compos. Sci. Technol.* 181 (2019) 107688.
5 <https://doi.org/10.1016/j.compscitech.2019.107688>.
- 6 [24] T.E. Shelton, Z.A. Willburn, C.R. Hartsfield, G.R. Cobb, J.T. Cerri, R.A. Kemnitz,
7 Effects of thermal process parameters on mechanical interlayer strength for
8 additively manufactured Ultem 9085, *Polym. Test.* 81 (2020) 106255.
9 <https://doi.org/10.1016/j.polymertesting.2019.106255>.
- 10 [25] T. Liu, X. Tian, M. Zhang, D. Abliz, D. Li, G. Ziegmann, Interfacial performance
11 and fracture patterns of 3D printed continuous carbon fiber with sizing reinforced
12 PA6 composites, *Compos, Part A Appl. Sci.* 114 (2018) 368-376.
13 <https://doi.org/10.1016/j.compositesa.2018.09.001>.
- 14 [26] X. Tian, T. Liu, C. Yang, Q. Wang, D. Li, Interface and performance of 3D printed
15 continuous carbon fiber reinforced PLA composites, *Compos, Part A Appl. Sci.* 88
16 (2016) 198-205. <https://doi.org/10.1016/j.compositesa.2016.05.032>.
- 17 [27] P. Wang, B. Zou, S. Ding, L. Li, C. Huang, Effects of FDM-3D printing parameters
18 on mechanical properties and microstructure of CF/PEEK and GF/PEEK, *Chin. J.*
19 *Aeronaut.* 34(9) (2021) 236-246. <https://doi.org/10.1016/j.cja.2020.05.040>.
- 20 [28] Y. Ming, S. Zhang, W. Han, B. Wang, Y. Duan, H. Xiao, Investigation on process
21 parameters of 3D printed continuous carbon fiber-reinforced thermosetting epoxy
22 composites, *Addit. Manuf.* 33 (2020) 101184.
23 <https://doi.org/10.1016/j.addma.2020.101184>.
- 24 [29] J.E. Seppala, S. Hoon Han, K.E. Hillgartner, C.S. Davis, K.B. Migler, Weld
25 formation during material extrusion additive manufacturing, *Soft Matter* 13(38)
26 (2017) 6761-6769. <https://doi.org/10.1039/C7SM00950J>.
- 27 [30] A.C. Abbott, G.P. Tandon, R.L. Bradford, H. Koerner, J.W. Baur, Process-
28 structure-property effects on ABS bond strength in fused filament fabrication, *Addit.*

1 Manuf. 19 (2018) 29-38. <https://doi.org/10.1016/j.addma.2017.11.002>.

2 [31] J. Yin, C. Lu, J. Fu, Y. Huang, Y. Zheng, Interfacial bonding during multi-material
3 fused deposition modeling (FDM) process due to inter-molecular diffusion, Mater.
4 Des. 150 (2018) 104-112. <https://doi.org/10.1016/j.matdes.2018.04.029>.

5 [32] N. Sabyrov, A. Abilgazyev, M.H. Ali, Enhancing interlayer bonding strength of
6 FDM 3D printing technology by diode laser-assisted system, Int. J. Adv. Manuf.
7 Tech. 108(1-2) (2020) 603-611. <https://doi.org/10.1007/s00170-020-05455-y>.

8 [33] M. Luo, X. Tian, J. Shang, W. Zhu, D. Li, Y. Qin, Impregnation and interlayer
9 bonding behaviours of 3D-printed continuous carbon-fiber-reinforced poly-ether-
10 ether-ketone composites, Compos, Part A Appl. Sci. 121 (2019) 130-138.
11 <https://doi.org/10.1016/j.compositesa.2019.03.020>.

12 [34] N. Aliheidari, R. Tripuraneni, A. Ameli, S. Nadimpalli, Fracture resistance
13 measurement of fused deposition modeling 3D printed polymers, Polym. Test. 60
14 (2017) 94-101. <https://doi.org/10.1016/j.polymertesting.2017.03.016>.

15 [35] D. Young, N. Wetmore, M. Czabaj, Interlayer fracture toughness of additively
16 manufactured unreinforced and carbon-fiber-reinforced acrylonitrile butadiene
17 styrene, Addit. Manuf. 22 (2018) 508-515.
18 <https://doi.org/10.1016/j.addma.2018.02.023>.

19 [36] S.S. Dasari, A. Sarmah, R.D. Mee, A.N. Khalfaoui, M.J. Green, Joule Heating of
20 Carbon Fibers and Their Composites in Radio-Frequency Fields, Adv. Eng. Mater.
21 25(10) (2023) 2201631. <https://doi.org/10.1002/adem.202201631>.

22 [37] R.D. Mee, A.G. Crowley, M.M. Mustafa, M.J. Green, Electric fields and local
23 heating in additively manufactured nanocomposite parts, Nanocomposites 9(1)
24 (2023) 43-49. <https://doi.org/10.1080/20550324.2023.2229187>.

25 [38] L. García-Guzmán, L. Távara, J. Reinoso, J. Justo, F. París, Fracture resistance of
26 3D printed adhesively bonded DCB composite specimens using structured
27 interfaces: Experimental and theoretical study, Compos. Struct. 188 (2018) 173-184.
28 <https://doi.org/10.1016/j.compstruct.2017.12.055>.

- 1 [39] N. Naat, Y. Boutar, S. Naïmi, S. Mezlini, L.F.M. Da Silva, Effect of surface texture
2 on the mechanical performance of bonded joints: a review, *The Journal of Adhesion*
3 99(2) (2021) 166-258. <https://doi.org/10.1080/00218464.2021.2008370>.
- 4 [40] M.T. Aranda, J. Reinoso, I.G. García, On different 3D printing methods and
5 fracture performance in DCB composite specimens including structured interfaces,
6 *Theor. Appl. Fract. Mech.* 122 (2022) 103552.
7 <https://doi.org/10.1016/j.tafmec.2022.103552>.
- 8 [41] S.E. Naleway, M.M. Porter, J. McKittrick, M.A. Meyers, Structural design
9 elements in biological materials: application to bioinspiration, *Adv. Mater.* 27(37)
10 (2015) 5455-5476. <https://doi.org/10.1002/adma.201502403>.
- 11 [42] B. Zhang, Q. Han, J. Zhang, Z. Han, S. Niu, L. Ren, Advanced bio-inspired
12 structural materials: Local properties determine overall performance, *Mater. Today*
13 41 (2020) 177-199. <https://doi.org/10.1016/j.mattod.2020.04.009>.
- 14 [43] N. Lee, M.F. Horstemeyer, H. Rhee, B. Nabors, J. Liao, L.N. Williams,
15 Hierarchical multiscale structure–property relationships of the red-bellied
16 woodpecker (*Melanerpes carolinus*) beak, *J. R. Soc. Interface* 11(96) (2014)
17 20140274. <https://doi.org/10.1098/rsif.2014.0274>.
- 18 [44] J. Wang, D. Hu, Z. Zhang, B. Pei, R. Xu, X. Wu, Anti-impact performance of bionic
19 tortoiseshell-like composites, *Compos. Struct.* 303 (2023) 116315.
20 <https://doi.org/10.1016/j.compstruct.2022.116315>.
- 21 [45] N.A. Yaraghi, N. Guarín-Zapata, L.K. Grunenfelder, E. Hintsala, S. Bhowmick,
22 J.M. Hiller, M. Betts, E.L. Principe, J.Y. Jung, L. Sheppard, R. Wuhler, J.
23 McKittrick, P.D. Zavattieri, D. Kisailus, A Sinusoidally Architected Helicoidal
24 Biocomposite, *Adv. Mater.* 28(32) (2016) 6835-44.
25 <https://doi.org/10.1002/adma.201600786>.
- 26 [46] F.A. Cordisco, P.D. Zavattieri, L.G. Hector, B.E. Carlson, Mode I fracture along
27 adhesively bonded sinusoidal interfaces, *Int. J. Solids Struct.* 83 (2016) 45-64.
28 <https://doi.org/10.1016/j.ijsolstr.2015.12.028>.

- 1 [47] K. Xu, Y. Li, L. Chen, K. Tang, Curved layer based process planning for multi-
2 axis volume printing of freeform parts, *Comput. Aided Des.* 114 (2019) 51-63.
3 <https://doi.org/10.1016/j.cad.2019.05.007>.
- 4 [48] F. Xie, D. Bi, K. Tang, A potential field based multi-axis printing path generation
5 algorithm, *Int. J. Computer Integr. Manuf.* 33(12) (2020) 1277-1299.
6 <https://doi.org/10.1080/0951192x.2020.1815851>.
- 7 [49] Y. Li, D. He, S. Yuan, K. Tang, J. Zhu, Vector field-based curved layer slicing and
8 path planning for multi-axis printing, *Rob. Comput. Integr. Manuf.* 77 (2022)
9 102362. <https://doi.org/10.1016/j.rcim.2022.102362>.
- 10 [50] F. Wulle, O. Gorke, S. Schmidt, M. Nistler, G.E.M. Tovar, O. Riedel, A. Verl, A.
11 Weber, A. Southan, Multi-axis 3D printing of gelatin methacryloyl hydrogels on a
12 non-planar surface obtained from magnetic resonance imaging, *Addit. Manuf.* 50
13 (2022) 102566. <https://doi.org/10.1016/j.addma.2021.102566>.
- 14 [51] Y. Li, K. Tang, D. He, X. Wang, Multi-axis support-free printing of freeform parts
15 with lattice infill structures, *Comput. Aided Des.* 133 (2021) 102986.
16 <https://doi.org/10.1016/j.cad.2020.102986>.
- 17 [52] J. Naranjo-Lozada, H. Ahuett-Garza, P. Orta-Castañón, W.M.H. Verbeeten, D.
18 Sáiz-González, Tensile properties and failure behavior of chopped and continuous
19 carbon fiber composites produced by additive manufacturing, *Addit. Manuf.* 26
20 (2019) 227-241. <https://doi.org/10.1016/j.addma.2018.12.020>.
- 21 [53] B.P. Heller, D.E. Smith, D.A. Jack, Planar deposition flow modeling of fiber filled
22 composites in large area additive manufacturing, *Addit. Manuf.* 25 (2019) 227-238.
23 <https://doi.org/10.1016/j.addma.2018.10.031>.
- 24 [54] ASTM D5528M–21, Standard test method for mode I interlaminar fracture
25 toughness of unidirectional fiber-reinforced polymer matrix composites; 2021.
- 26 [55] ASTM D7905M-19, Standard test method for determination of the mode II
27 interlaminar fracture toughness of unidirectional fiber-reinforced polymer matrix
28 composites; 2019.

- 1 [56] R.J.A. Allen, R.S. Trask, An experimental demonstration of effective Curved Layer
2 Fused Filament Fabrication utilising a parallel deposition robot, *Addit. Manuf.* 8
3 (2015) 78-87. <https://doi.org/10.1016/j.addma.2015.09.001>.
- 4 [57] J.R. Kubalak, A.L. Wicks, C.B. Williams, Exploring multi-axis material extrusion
5 additive manufacturing for improving mechanical properties of printed parts, *Rapid*
6 *Prototyping J.* 25(2) (2019) 356-362. <https://doi.org/10.1108/rpj-02-2018-0035>.
- 7 [58] G.M. Fortunato, M. Nicoletta, E. Batoni, G. Vozzi, C. De Maria, A fully automatic
8 non-planar slicing algorithm for the additive manufacturing of complex geometries,
9 *Addit. Manuf.* 69 (2023) 103541. <https://doi.org/10.1016/j.addma.2023.103541>.
- 10 [59] K.-M.M. Tam, C.T. Mueller, Additive Manufacturing Along Principal Stress Lines,
11 *3D Print. Addit. Manuf.* 4(2) (2017) 63-81. <https://doi.org/10.1089/3dp.2017.0001>.
- 12 [60] J.R. Kubalak, A.L. Wicks, C.B. Williams, Using multi-axis material extrusion to
13 improve mechanical properties through surface reinforcement, *Virtual Phys. Prototy.*
14 13(1) (2018) 32-38. <https://doi.org/10.1080/17452759.2017.1392686>.
- 15 [61] G. Fang, T. Zhang, S. Zhong, X. Chen, Z. Zhong, C.C.L. Wang, Reinforced FDM:
16 Multi-Axis Filament Alignment with Controlled Anisotropic Strength, *ACM Trans.*
17 *Graphics* 39(6) (2020) 1-15. <https://doi.org/10.1145/3414685.3417834>.
- 18 [62] Y. Zhou, Y. Xiao, Q. Wu, Y. Xue, A multi-state progressive cohesive law for the
19 prediction of unstable propagation and arrest of Mode-I delamination cracks in
20 composite laminates, *Eng. Fract. Mech.* 248 (2021) 107684.
21 <https://doi.org/10.1016/j.engfracmech.2021.107684>.
- 22 [63] L.K. Jain, K.A. Dransfield, Y.-W. Mai, Effect of Reinforcing Tabs on the Mode I
23 Delamination Toughness of Stitched CFRPs, *J. Compos. Mater.* 32(22) (1998)
24 2016-2041. <https://doi.org/10.1177/002199839803202202>.
- 25 [64] J.R. Reeder, K. Demarco, K.S. Whitley, The use of doubler reinforcement in
26 delamination toughness testing, *Compos, Part A Appl. Sci.* 35(11) (2004) 1337-
27 1344. <https://doi.org/10.1016/j.compositesa.2004.02.021>.
- 28 [65] Y. Long, Z. Zhang, K. Fu, Y. Li, Efficient plant fibre yarn pre-treatment for 3D

- 1 printed continuous flax fibre/poly(lactic) acid composites, *Compos, Part B: Eng.*
2 227 (2021) 109389. <https://doi.org/10.1016/j.compositesb.2021.109389>.
- 3 [66] Z. Wang, Y. Li, H. Tu, The mode II interlaminar fracture toughness and healing
4 efficiency of repeatable self-healing composite, *Compos, Part A Appl. Sci.* 161
5 (2022) 107096. <https://doi.org/10.1016/j.compositesa.2022.107096>.
- 6 [67] M. Iragi, C. Pascual-González, A. Esnaola, C.S. Lopes, L. Aretxabaleta, Ply and
7 interlaminar behaviours of 3D printed continuous carbon fibre-reinforced
8 thermoplastic laminates; effects of processing conditions and microstructure, *Addit.*
9 *Manuf.* 30 (2019) 100884. <https://doi.org/10.1016/j.addma.2019.100884>.
- 10 [68] D. Yang, H. Zhang, J. Wu, E.D. McCarthy, Fibre flow and void formation in 3D
11 printing of short-fibre reinforced thermoplastic composites: An experimental
12 benchmark exercise, *Addit. Manuf.* 37 (2021) 101686.
13 <https://doi.org/10.1016/j.addma.2020.101686>.
- 14 [69] A. Srivastava, S. Osovski, A. Needleman, Engineering the crack path by
15 controlling the microstructure, *J. Mech. Phys. Solids* 100 (2017) 1-20.
16 <https://doi.org/10.1016/j.jmps.2016.12.006>.